Ensemble Spread Grows More Rapidly in Higher-Resolution Simulations of Deep Convection

JONATHAN A. WEYN AND DALE R. DURRAN

Department of Atmospheric Sciences, University of Washington, Seattle, Washington

(Manuscript received 7 November 2017, in final form 25 July 2018)

ABSTRACT

Idealized ensemble simulations of mesoscale convective systems (MCSs) with horizontal grid spacings of 1, 1.4, and 2 km are used to analyze the influence of numerical resolution on the rate of growth of ensemble spread in convection-resolving numerical models. The ensembles are initialized with random phases of 91-km-wavelength moisture perturbations that are captured with essentially identical accuracy at all resolutions. The rate of growth of ensemble variance is shown to systematically increase at higher resolution. The largest horizontal wavelength at which the perturbation kinetic energy (KE′) grows to at least 50% of the background kinetic energy spectrum is also shown to grow more rapidly at higher resolution. The mechanism by which the presence of smaller scales accelerates the upscale growth of KE′ is clear-cut in the smooth-saturation Lorenz–Rotunno–Snyder (ssLRS) model of homogeneous surface quasigeostrophic turbulence. Comparing the growth of KE′ from the MCS ensemble simulations to that in the ssLRS model suggests interactions between perturbations at small scales, where KE′ is not yet completely saturated, and somewhat larger scales, where KE′ is clearly unsaturated, are responsible for the faster growth rate of ensemble variance at finer resolution. These results provide some empirical justification for the use of deep-convection-related stochastic parameterization schemes to reduce the problem of underdispersion in coarser-resolution ensemble prediction systems.

1. Introduction

Ensemble forecasting provides a way of accounting for the inherent uncertainty in numerical weather forecasts. One major source of such uncertainty arises from the inaccurate specification of initial conditions, and one of the most important ways of forming an ensemble is to generate a set of numerical simulations by starting from a set of plausible, but slightly different, initial conditions. As the forecasts from such initial-condition ensembles proceed, the ensemble typically becomes underdispersive in the sense that the spread among the ensemble members becomes too small to ensure that the verifying weather pattern is contained within the ensemble (e.g., Buizza et al. 2005; Raftery et al. 2005; Schwartz et al. 2014).

Several empirical methods have been proposed to increase ensemble spread and thereby reduce the problem of underdispersion, including stochastically perturbed parameterization tendencies (SPPT; Buizza et al. 1999) and stochastic kinetic energy backscatter (SKEB; Shutts 2005). At the European Centre for Medium-Range Weather Forecasts (ECMWF), SKEB is implemented in a configuration designed to account for unresolved deep convection in a manner conceptually similar to another alternative for increasing ensemble spread, the stochastic convective backscatter (SCB) algorithm (Shutts 2015). It has been supposed that if the spatial resolution is increased to the point where interactions between the convection and larger scales can be explicitly resolved, the need for parameterizations such as the ECMWF-type SKEB and SCB should be reduced (Leutbecher et al. 2017).

The assumption that SCB and ECMWF-type SKEB become less important at higher resolution is supported by previous studies following the evolution of pairs of simulations with nearly identical initial conditions and showing that the difference between the twins (the error) increases faster in fine-resolution convection-permitting simulations than in coarser-resolution simulations using convective parameterizations. Zhang et al. (2003) found more rapid error growth in convection-permitting 3.3-km-resolution simulations than in 30-km simulations with parameterized convection. Hohenegger and Schär (2007) found an order of magnitude difference in the doubling time of global errors between synoptic-scale (80-km resolution) and

---

Corresponding author: Jonathan A. Weyn, jweyn@uw.edu

DOI: 10.1175/JAS-D-17-0332.1

cloud-resolving (2.2-km resolution) models. Moving beyond pairs of near-twin experiments, similar results were obtained for larger ensembles by Clark et al. (2009, 2010), who showed that ensemble spread grows faster at convection-allowing 4-km resolution than at 20-km resolution with convective parameterization.

Deep convection is a highly nonlinear phenomenon with rapid error growth rates and short eddy turnover times. Consistent with these previous results, models with sufficient resolution to at least approximately include convective dynamics might naturally be expected to generate more rapid growth of ensemble spread than coarser-resolution models that rely on convective parameterizations. But how does the ensemble spread compare when all model simulations use a horizontal grid spacing sufficient to capture the basic dynamics of deep convection? Generalizing from the seminal idealized-model analysis of Lorenz (1969), differences between ensemble members are expected to grow most rapidly at the smallest scales. In particular, in homogeneous isotropic turbulence, dimensional analysis suggests that the kinetic energy of the perturbations about the ensemble mean (KE′) will grow at eddy turnover time scales that decrease as the wavelength of the perturbations decreases, provided the slope of the background kinetic energy (KE) spectrum is shallower than k^{-3}, where k is the wavenumber (Lorenz 1969; Lilly 1972; Palmer et al. 2014). Although deep convection is not homogeneous isotropic turbulence, the atmospheric kinetic energy spectrum has a $k^{-5/3}$ slope at the wavelengths characteristic of deep convection, and previous ensemble simulations of deep convection have verified expectations that the KE′ spectrum grows fastest at the smallest scales (Weyn and Durran 2017, hereafter WD17).

Nevertheless, the overall effect of numerical resolution on upscale KE′ growth is not immediately obvious. Suppose convection is being forecast with models having horizontal grid spacings of either 1 or 2 km and that, owing to the limitations of the data-assimilation procedure, the initial KE′ spectrum for both ensembles is saturated at all scales shorter than 8 km but is very small at all larger scales. Will the different spatial resolutions make a difference in the time required for KE′ at 16 km to become saturated in each ensemble? To the extent that KE′ grows to larger scales through a cascade involving just a few slightly shorter wavelengths, the smallest-scale contributions to KE′ in the higher-resolution model may not be of practical importance, and there may be little difference between the ensembles in the upscale growth of KE′.

To better illustrate the issue in the preceding question, Fig. 1 shows the evolution of the KE′ spectra in a close relative of Lorenz's original 1969 turbulence model, the smooth-saturation Lorenz–Rotunno–Snyder (ssLRS) model (Durran and Gingrich 2014), configured for surface quasigeostrophic dynamics (Rotunno and Snyder 2008).[1] The initial error is localized at the smallest retained wavelength of approximately 1 km (dashed blue curve), and the classic upscale cascade of initial errors is clearly apparent, with the most rapidly growing errors at any time having maximum amplitude at scales just slightly larger than those that are saturated. Now suppose that the initial KE′ spectrum is given instead by the dashed orange curve in Fig. 1 (which is the level to which errors would grow in 6 h if the initial KE′ distribution followed the dashed blue curve). That orange curve shows KE′ saturated at all scales for which k exceeds $10^{-3}\,\mathrm{m}^{-1}$. Suppose the cutoff wavelength in one ensemble is at 1 km (the end of the heavy black line at wavenumber $6.3\times10^{-3}\,\mathrm{m}^{-1}$) and the cutoff wavelength for the second ensemble is at 2 km; in the context of the ssLRS model, our previous question is, For which ensemble will the KE′ spectrum grow most rapidly upscale and approach the dashed green curve?

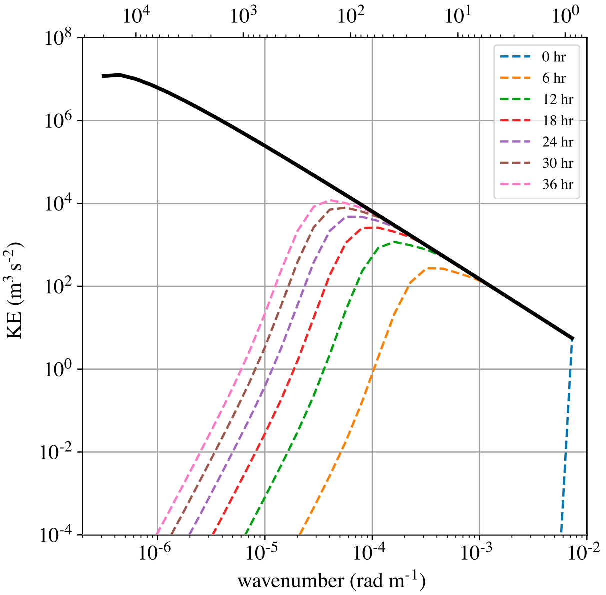

FIG. 1. Evolution of the perturbation KE spectrum plotted at 6-h intervals (colored dashed lines; $\mathrm{m^3\,s^{-2}}$) for the ssLRS model when the initial error spectrum is saturated at the shortest retained wavelength and negligible at all longer wavelengths. The thick black line indicates the background saturation spectrum used by Lorenz, which is proportional to $k^{-5/3}$ except at the planetary scales.

---

[1] More details of about the ssLRS model are provided in section 4.

In this paper, we examine the influence of numerical resolution on the rate at which differences among ensemble members due to initial-condition perturbations increase in simulations of idealized mesoscale convective systems (MCSs) and in the ssLRS model of homogeneous surface quasigeostrophic turbulence. The rest of this paper is organized as follows. Section 2 provides details about the model configuration and the initial perturbations imposed to create ensembles of simulated MCSs. Section 3 describes an analysis of the perturbation growth and ensemble spread in the MCS simulations. Section 4 compares the upscale growth of initial perturbations in the MCS simulations with that in the ssLRS model. Last, section 5 contains the conclusions.

2. Model configuration and simulation strategy

The model configuration closely follows that in WD17. The same nonhydrostatic cloud-resolving model is used to generate ensembles of 1 control and 20 perturbed members, each at horizontal grid spacings of 1, 1.4, and 2 km. Additionally, an ensemble with 1-km grid spacing and quadrupled fourth-order numerical diffusion, designated "1 km-D," is also included. The smallest resolvable wave (having a wavelength of $2\Delta x$) is effectively removed every 2.5 time steps in the 1-km-D simulation. The background thermodynamic profile used to initialize the model is identical to that of WD17, as is the vertical wind profile, except that the westerly wind is a constant 25 m s^{-1} above the layer of linear wind shear between the surface and 5 km. Individual simulations are made on a 512 km × 512 km square doubly periodic horizontal domain. The number of grid points in the x and y directions varies based on the resolution, with 512, 366, and 256 grid points at 1, 1.4, and 2 km, respectively. The integration time step is 2, 3, and 4 s at grid spacings of 1, 1.4, and 2 km, respectively. In all ensemble members, three identical bubbles 2 K warmer than the environment produce the initial updrafts, which subsequently evolve into an organized MCS owing to the wind shear. The bubbles are spheroidal with a 20-km horizontal radius and 1.4-km vertical radius, centered 1.4 km above the surface at (x, y) locations of (100, 250), (125, 175), and (150, 300) km. All other details of the model are as in WD17.

The synthetic composite reflectivity for the unperturbed control members in the 1-km, 1-km-D, and 1.4- and 2-km simulations are shown at 5 h in Fig. 2. In all cases, a strong north–south-oriented line of thunderstorms has developed. The reflectivity fields are very similar, with modest increases in the north–south extent of the line and losses in fine structure appearing as the grid spacing or the numerical smoothing increases; there are no major changes to the MCS structure or convective dynamics because of the differences in resolution.[2]

The control members are unperturbed, while the other ensemble members have initial perturbations added to the water vapor mixing ratio field in the form

$$q_v = ae^{-z/H}\sin\left[2\pi\left(\frac{x}{L}-\phi_x\right)\right]\sin\left[2\pi\left(\frac{y}{L}-\phi_y\right)\right], \quad (1)$$

where the amplitude is $a = 0.1\,\mathrm{g\,kg^{-1}}$; $L = 128$ km, giving a two-dimensional horizontal wavelength of 90.5 km; and the vertical e-folding decay scale is $H = 1$ km. The phases ϕ_x and ϕ_y $(0 \le \phi < 2\pi)$ are generated randomly for each ensemble member, and hence, the differences between ensemble members originate in the difference in phase between the perturbations and the initial warm bubbles.

The initial perturbations are imposed on large scales for three reasons. First, it eliminates the sensitivity to the otherwise arbitrary factor by which the scale of the initial-condition perturbations exceeds the horizontal grid spacing in the different ensembles by making that factor very large. Second, it eliminates the sensitivity of the initial-condition perturbations to numerical dissipation; for example, if the initial perturbations were imposed at 8 km, this would be a $4\Delta x$ wavelength in the 2-km ensemble and immediately subject to much more numerical dissipation than in the 1-km ensemble, where it would have a wavelength of $8\Delta x$. Finally, the third reason for imposing large-scale initial perturbations is that these may be a more important source of uncertainty than perturbations on the smallest resolved scales in very-high-resolution mesoscale models. In particular, recent work (Durran and Gingrich 2014; Durran and Weyn 2016; WD17) has highlighted a little-known result in Lorenz (1969) suggesting that initial large-scale errors can be as detrimental to forecasts as initial small-scale errors of the same absolute amplitude. Morss et al. (2009) used a similar strategy of imposing initial perturbations at large scales in an investigation of the influence of spatial resolution on the growth of perturbation KE in a dry quasigeostrophic model.

In addition to the ensembles with moisture perturbations present in the initial conditions, another set of ensembles is constructed by adding the same moisture perturbations when the MCSs and background circulations are well established, at 4 h into the simulation, thereby allowing the analysis of perturbation growth in a complex background state.

---

[2] Additional simulations with a horizontal grid spacing of 2.8 km were also performed. These showed some important differences from the rest of the simulations and are discussed further in appendix B.

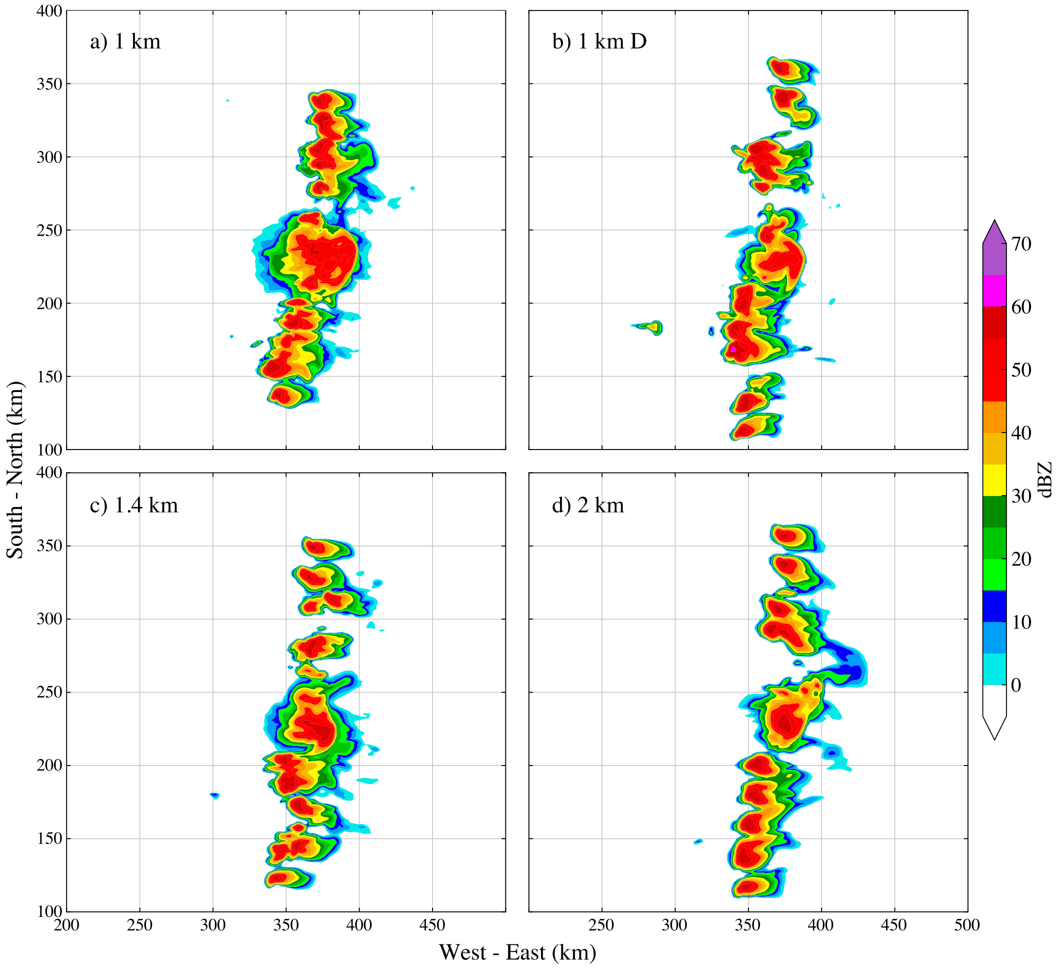

FIG. 2. The 5-h synthetic composite reflectivity for the control member of the (a) 1-km, (b) 1-km-D, c) 1.4-km, and (d) 2-km ensembles. There is no convection outside of the subset of the domain shown.

3. The MCS ensembles

To gain physical intuition about the spread of perturbations in the 1-, 1.4-, and 2-km ensemble simulations, the agreement among the members on the location of strong convective elements is shown in Fig. 3, which contours the number of ensemble members, including the control, having synthetic reflectivity matching or exceeding 45 dBZ at each spatial point. At $t = 3$ h into the simulations, there are a relatively large number of members in agreement on the locations of most convective cells. Nevertheless, the spread clearly decreases with increasing grid spacing, with the 2-km ensemble exhibiting nearly perfect alignment of every significant high-reflectivity cell. By $t = 5$ h, however, there is much less certainty in the location of the strongest convection in the 1-km ensemble, where there is a wide swath of points at which only 9–13 members agree on the location of the high-reflectivity cells. At 2-km resolution, on the other hand, the locations of these cells are much more similar across the ensemble members. At both 3 and 5 h, the spread in the 1.4-km ensemble lies in between that in the 1- and 2-km cases.

a. Growth of ensemble variance

The domain-averaged ensemble variance of a variable ϕ is

$$\mathrm{Var}(\phi) = \frac{1}{n_x n_y n_e} \sum_{i=1}^{n_x} \sum_{j=1}^{n_y} \sum_{m=1}^{n_e} (\phi_{i,j,m} - \overline{\phi_{i,j}})^2 , \qquad (2)$$

where $\phi_{i,j,m}$ is the value at gridpoint (i, j) in the mth ensemble member, the overbar denotes the ensemble mean (excluding the control), and the summation is over all $n_e = 20$ ensemble members and over all n_x and n_y grid indices along the x and y coordinates. The evolution of domain-averaged ensemble variance of hourly accumulated precipitation, water vapor mixing

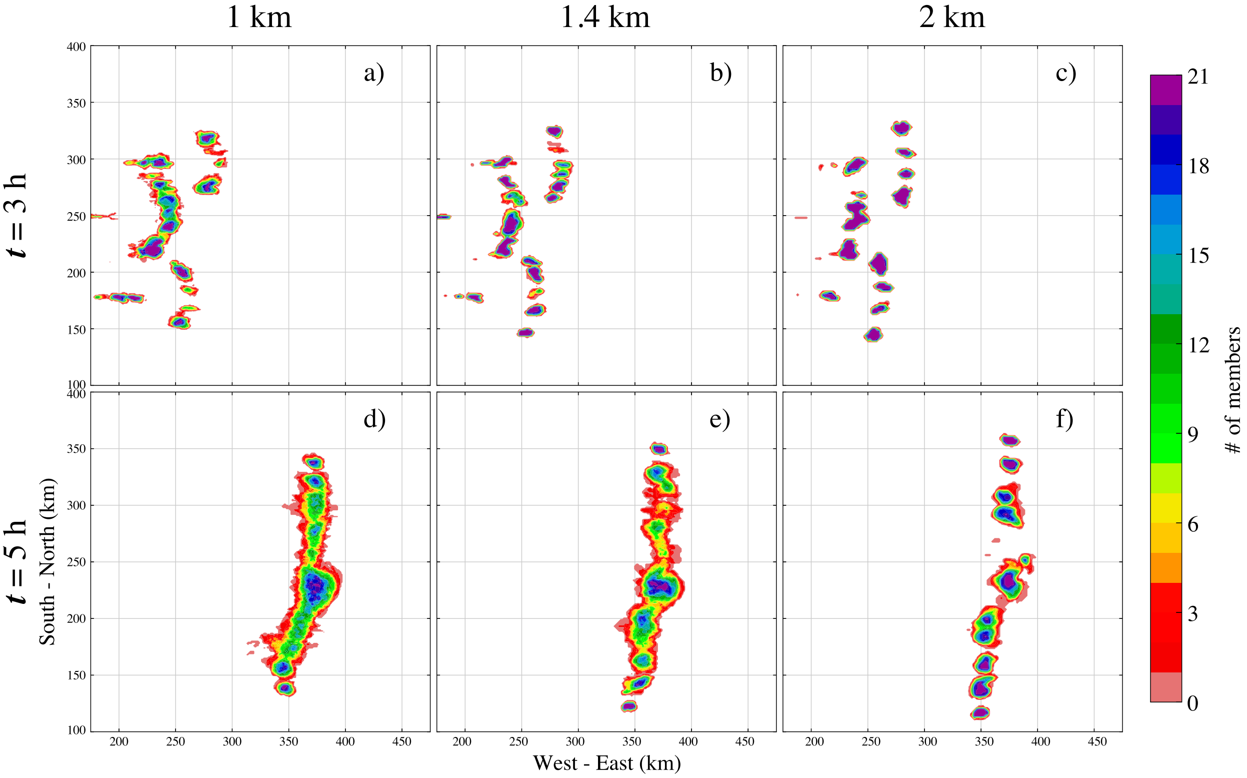

FIG. 3. Number of ensemble members (including control, giving a total of 21 members) matching or exceeding a synthetic reflectivity value of 45 dBZ at each point in the (a),(d) 1-, (b),(e) 1.4-, and (c),(f) 2-km ensembles at simulation times of (a)–(c) $t = 3$ and (d)–(f) $t = 5$ h.

ratio q_v at a height of $z = 2$ km, and potential temperature θ at $z = 2$ km is shown in Fig. 4 for the ensembles with 1-, 1.4-, and 2-km horizontal grid spacing. Variance increases roughly exponentially at times up to about $t = 3$ h ($t = 4$ h for precipitation) and approximately linearly afterward. In general, the variance and its growth rate decreases as the horizontal grid spacing increases, and the differences over the first 4 h are statistically significant. An exception appears in the variance of q_v for the 1.4-km ensemble, which exceeds that for the 1-km ensemble after 4 h. The variance in hourly precipitation increases particularly smoothly because every point (plotted at 10-min intervals) contains the accumulated precipitation over the previous 60 min.

To more quantitatively assess the dependence of the growth rate of domain-averaged ensemble variance on numerical resolution, Fig. 5 shows the evolution of Var(q_v) at $z = 2$ km (blue curves) from each ensemble on a logarithmic scale. After about 1 h, log[Var(q_v)] increases almost linearly for a period of 2–3 h. For each ensemble, a least squares linear fit is calculated to log[Var(q_v)] beginning at 1 h into the simulations and ending at the first subsequent time for which the slope starts decreasing.[3] The doubling time for Var(q_v) is calculated for each ensemble from the slope of this linear fit and displayed, along with the standard deviation computed from the slopes of the individual ensemble members, in each panel of Fig. 5. These doubling times increase consistently with increases in horizontal grid spacing, and the differences between the doubling times at each step up in the grid spacing exceeds twice the standard deviation. While changes to the horizontal grid spacing of the model clearly result in faster ensemble spread at higher resolution, the 1-km-D simulations with increased diffusion have a doubling time very close to the 1.4-km simulations, suggesting that the factor-of-4 increase in numerical smoothing in the 1-km-D runs hinders the growth of Var(q_v) in a similar manner to coarsening the resolution by a factor of $\sqrt{2}$.

---

[3] Sensitivity tests where the slopes where calculated over hours 1–3 for all ensembles gave the same statistically significant relative rankings of the ensembles.

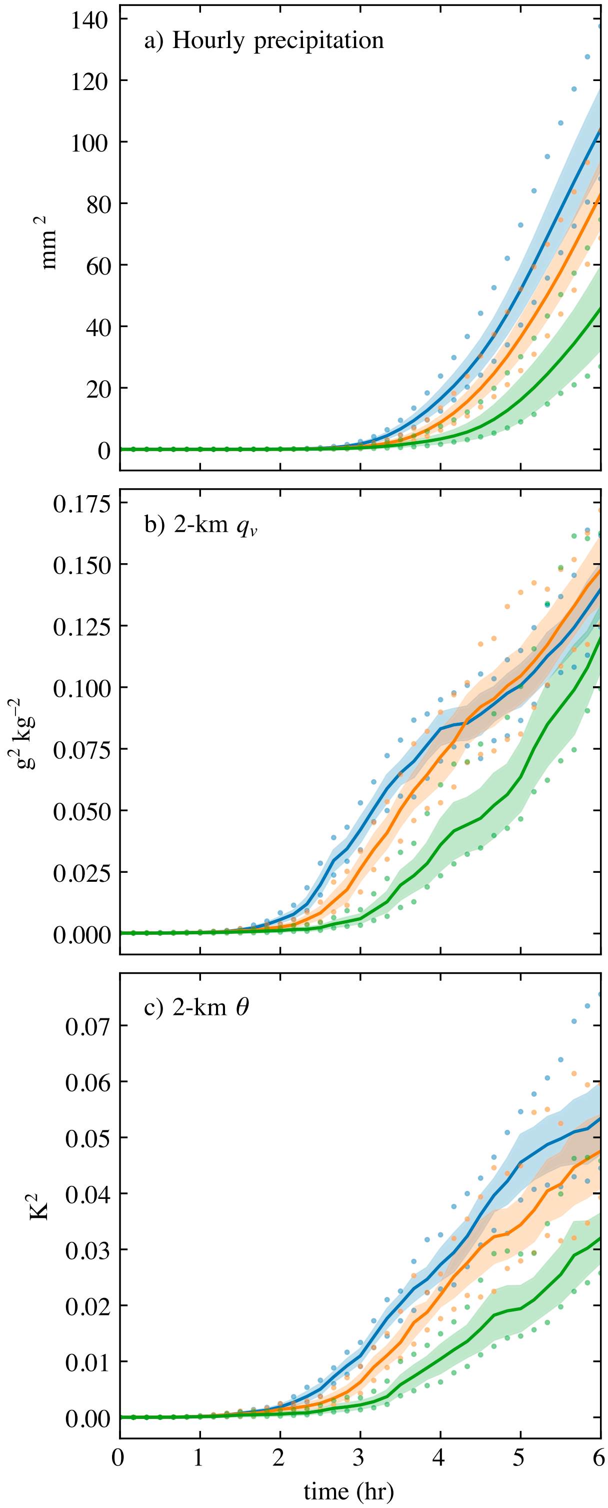

FIG. 4. Variance about the ensemble mean in (a) precipitation accumulated over the last hour (mm^2), (b) water vapor mixing ratio at a height of $z = 2$ km ($\mathrm{g}^2\,\mathrm{kg}^{-2}$), and (c) potential temperature at $z = 2$ km (K^2) for the 1- (blue), 1.4- (orange), and 2-km (green) ensembles. Solid lines indicate the ensemble mean, dots indicate the maximum and minimum ensemble members, and the shading represents the range of one standard deviation from the mean.

In addition to the variance, Fig. 5 includes curves showing the evolution of the mean-square difference (MSD):

$$\mathrm{MSD}(\phi) = \frac{1}{n_x n_y n_e} \sum_{i=1}^{n_x} \sum_{j=1}^{n_y} \sum_{s=1}^{n_e} (\phi_{i,j,m} - \phi_{i,j}^c)^2 \,, \qquad (3)$$

where ϕ^c denotes the variable in the control run, and the square of the ensemble bias

$$\mathrm{Bias}^2(\phi) = \frac{1}{n_x n_y} \sum_{i=1}^{n_x} \sum_{j=1}^{n_y} (\overline{\phi_{i,j}} - \phi_{i,j}^c)^2 \,. \qquad (4)$$

The MSD is a measure of the error in the ensemble with respect to the unperturbed control simulation and is the sum of the variance and the square of the bias. Although the square of the bias grows more rapidly than the variance, as shown in Fig. 5, the contribution of $\mathrm{Var}(q_v)$ to $\mathrm{MSD}(q_v)$ dominates that of $\mathrm{Bias}^2(q_v)$ until about $t =$ 3 h, while after $t = 4$ h, $\mathrm{Var}(q_v)$ is approximately equal to $\mathrm{Bias}^2(q_v)$. Hence, the growth in ensemble spread is largely responsible for the initial growth of errors relative to the control, while at later times, the control member is statistically indistinguishable from any individual ensemble member. Spatial maps of $\mathrm{MSD}(q_v)$ at $t = 5$ h are shown for all ensembles in Fig. 6. Noting the logarithmically spaced contour intervals, these maps illustrate the dominant contribution from the region of active convection (cf. Fig. 2) to the total MSD in all cases. Figure 6 also shows that, while the total MSD is similar in magnitude across the ensembles, the locally highest values occur in the ensemble with 1.4-km grid spacing.

The rate at which $\mathrm{Var}(q_v)$ grows faster as the resolution is made finer is remarkably similar to that which can be obtained using dimensional analysis to compare the growth of KE′ at different scales in homogeneous turbulence. As discussed in Lilly (1972) and Palmer et al. (2014), if $E(k)$ denotes the background KE spectral density per unit wavenumber ($\mathrm{m}^3\,\mathrm{s}^{-2}$) in homogeneous isotropic turbulence, dimensional analysis yields a time scale for circulations at wavenumber k of

$$T(k) \propto k^{-3/2} E^{-1/2} \,.$$

Assuming E follows a power law such that $E \propto k^{-p}$ and that $T(k)$ is proportional to the time for the magnitude of perturbations in KE′ to double at wavenumber k, the ratio of doubling times for circulations of scale λ and $\alpha\lambda$ is

$$\frac{T(k)}{T(k/\alpha)} = \alpha^{(p-3)/2} \,. \qquad (5)$$

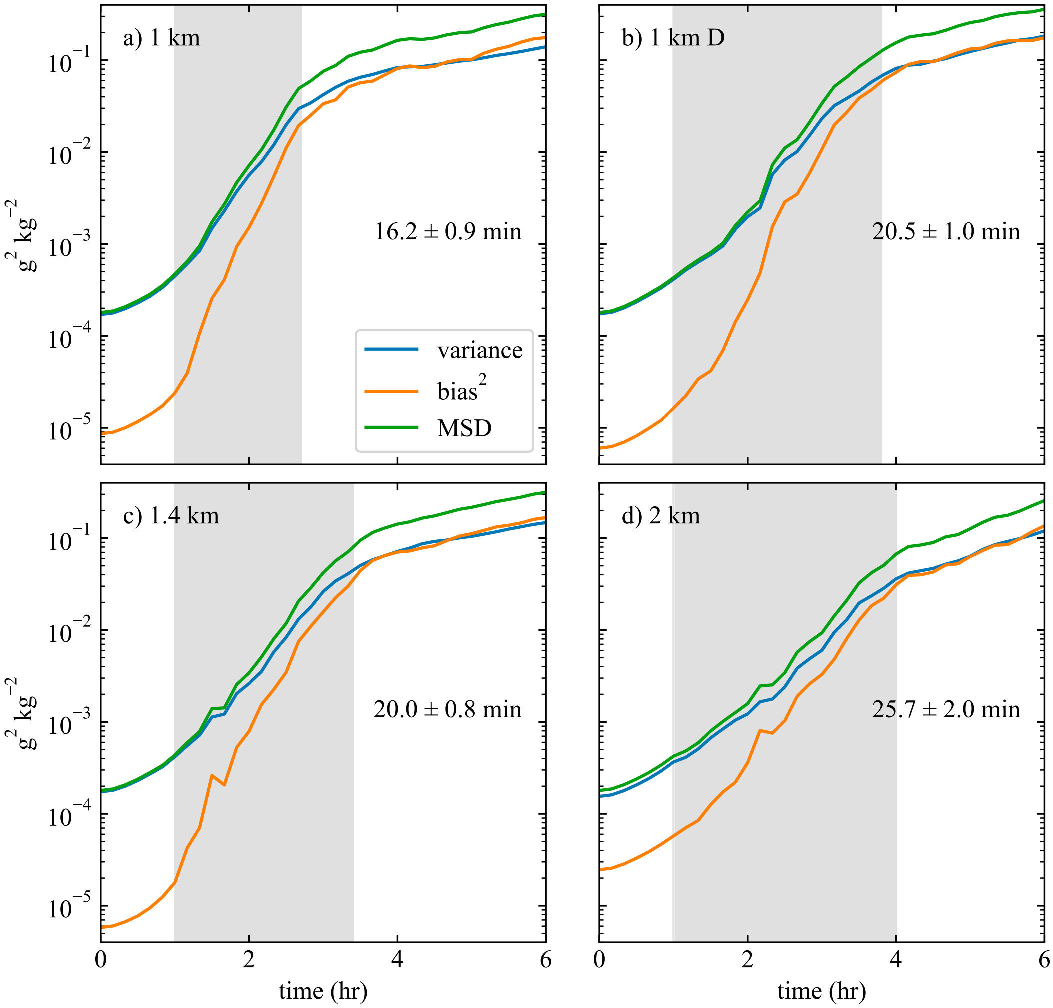

FIG. 5. Var(q_v) (blue), MSD(q_v) (green), and Bias^2(q_v) (orange) at $z = 2$ km as a function of time for the (a) 1-km, (b) 1-km-D, (c) 1.4-km, and (d) 2-km ensembles. The gray shading denotes the region where the linear fit was calculated to determine the variance doubling times, which are reported in the panels along with one-standard-deviation confidence intervals.

Similar to the cases discussed in WD17 (see their Fig. 6), the background KE spectra in all our ensembles develop a $k^{-5/3}$ slope by one hour into the simulation. Let r_α be the ratio in (5) for the case $E \propto k^{-5/3}$, then $r_\alpha = \alpha^{-2/3}$.

In Table 1, the ratios r_α for α equal to $\sqrt{2}$ and 2 are compared with the ratios of the variance doubling times given in Fig. 5 for the pair of 1.4- and 1-km simulations and the pair of 2- and 1-km simulations, respectively. The close agreement between the values of r_α and the ratios of the variance doubling times suggests that most of the ensemble spread in the water vapor field at these early times is produced by perturbations in the advective transport scaling with the grid resolution, that the scaling of this quantity (which is second-order in perturbation amplitude) works in a similar manner to the perturbation kinetic energy, and that dimensional analysis of this idealized system is at least roughly capable of modeling the growth of ensemble variance at early times in the simulations.[4]

b. Perturbation kinetic energy spectra and their approach to saturation

The evolution and approach to saturation of the perturbations in kinetic energy about the ensemble mean KE were evaluated as a function of horizontal scale by calculating the two-dimensional total and

---

[4] This result may only hold for a relatively narrow range of horizontal grid spacings where the dynamics of the system are not significantly affected by the numerical resolution; see appendix B.

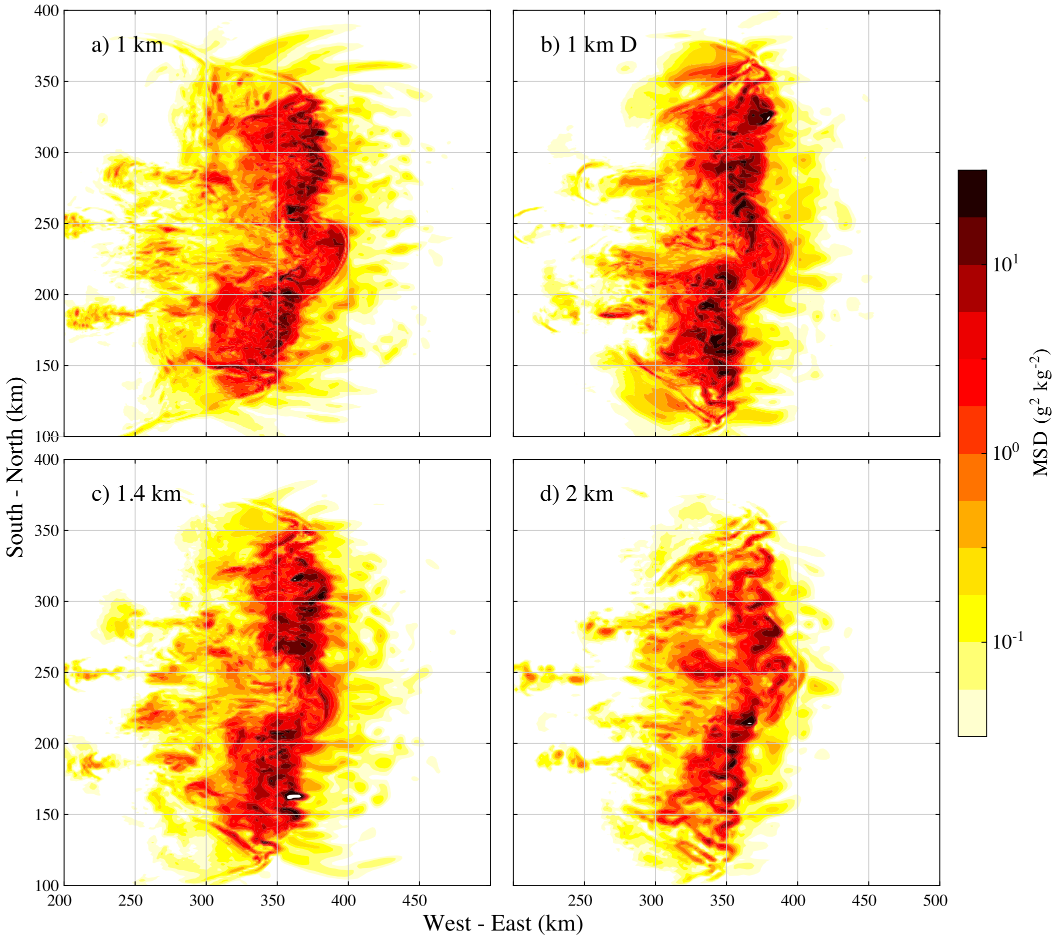

FIG. 6. Spatial maps of MSD(q_v) at $z = 2$ km and $t = 5$ h for the (a) 1-km, (b) 1-km-D, (c) 1.4-km, and (d) 2-km ensembles. Note the logarithmic spacing of the contour intervals and the white region around $(x, y) = (360, 160)$ km in (c) where the MSD exceeds the upper limit of the color scale.

perturbation kinetic energy spectral densities following WD17 and using the numpy.fft module in Python. At a given height and time, denoting the zonal and meridional velocities of the mth ensemble member as u_m and v_m, respectively, and denoting the two-dimensional discrete Fourier transform of a variable ϕ as $\hat{\phi}$ and its complex conjugate as $\hat{\phi}^*$, the total (background) KE spectral density is

$$\widehat{\mathrm{KE}}_m(k_h) = \frac{\Delta x \Delta y \Delta k}{8\pi^2 n_x n_y}[\hat{u}_m(k_h)\hat{u}^*_m(k_h) + \hat{v}_m(k_h)\hat{v}^*_m(k_h)], \tag{6}$$

where k_h is the magnitude of the 2D horizontal wavenumber; n_x and n_y are the number of grid points in the x and y directions, respectively; Δx and Δy are the horizontal grid spacing along those directions; and the leading coefficient in (6) is derived in Durran et al. (2017). The spectral density at each individual horizontal wavenumber pair (k_x, k_y) is added to the bin for which $k_h - \Delta k/2 < \sqrt{k_x^2 + k_y^2} \le k_h + \Delta k/2$, where $\Delta k = 2\pi/512\ \mathrm{km}^{-1}$ is the smallest resolved wavenumber, corresponding to the longest wavelength in the periodic domain. The perturbation kinetic energy spectral density $\widehat{\mathrm{KE}'_m}$ is also calculated from (6) except that the velocities are replaced by differences from the ensemble mean; that is, $u'_m = u_m - \overline{u}$, where the overbar denotes the ensemble mean. Computing perturbations about the ensemble mean follows Lorenz (1969) and reflects the growth in ensemble variance.[5] For comparison with the generalized Lorenz model, $\widehat{\mathrm{KE}}$ and $\widehat{\mathrm{KE}'}$ are computed as the average of $\widehat{\mathrm{KE}}_m$ and $\widehat{\mathrm{KE}'_m}$ over all ensemble members. The spectra are also scaled by a

---

[5] Essentially identical results are obtained if the perturbations are computed as differences from the unperturbed control member, rather than the ensemble mean, except that as saturation occurs, the perturbation KE values approach twice those of the background KE.

TABLE 1. Ratio of variance doubling times at different pairs of scales from the dimensional analysis of homogeneous turbulence r_α and as deduced from the simulations at different resolutions in Fig. 5.

Ratio of scales	Dimensional analysis	Simulations
1: $\sqrt{2}$	0.79	0.81
1:2	0.63	0.63

wavenumber-dependent compensating factor (Durran et al. 2017) to reduce systematic noise introduced by binning.

Spectra of perturbation and total KE from the 1- and 2-km simulations with initial-condition perturbations in the humidity at 91-km wavelength are shown in Fig. 7. These spectra are vertically averaged over the layer $0 \le z \le 16$ km. The $\widehat{\mathrm{KE}}'$ spectrum at scales larger than those directly influenced by numerical dissipation (i.e., larger than roughly $7\Delta x$) is relatively flat. In contrast to the upscale KE′ cascade apparent at small scales in Fig. 1, the perturbation KE grows primarily up-amplitude. At 1 h, $\widehat{\mathrm{KE}}'$ for the 1-km ensemble exceeds that of the 2-km ensemble on scales shorter than about 20 km, whereas values of $\widehat{\mathrm{KE}}'$ for both ensembles are quite similar at longer wavelengths. By 2 h, the differences have moved well upscale, with $\widehat{\mathrm{KE}}'$ for the 1-km ensemble exceeding that for the 2-km ensemble over scales up to roughly 200 km. At 3 h, $\widehat{\mathrm{KE}}'$ for the 1-km ensemble exceeds that for the 2-km case at all scales. By 6 h, the relative difference in $\widehat{\mathrm{KE}}'$ between the two ensembles is much less than at 3 h, and KE′ at the shortest wavelengths has saturated in both ensembles.

As an aggregate measure of the scale-dependent loss of predictability useful for interensemble comparisons, let λ_{50} be the maximum horizontal scale at which the 0–16-km vertically averaged $\widehat{\mathrm{KE}}'/\widehat{\mathrm{KE}}$ ratio exceeds 50%. Values of λ_{50} are plotted as a function of time for all ensembles in Fig. 8. As expected from previous studies (Lorenz 1969; Rotunno and Snyder 2008; Zhang et al. 2007; WD17), λ_{50} increases with time as $\widehat{\mathrm{KE}}'$ grows upscale. The fastest growth and highest values of λ_{50} at all but the latest times occur in the 1-km ensemble. As the horizontal grid spacing is increased, λ_{50} grows more slowly. The curve for the 1-km-D ensemble approximates that for the 1.4-km ensemble, again suggesting that numerical diffusion has a similar effect to a truncation of the resolved scales.

4. Interpretation via the ssLRS model

To investigate the influence of spatial resolution on the growth of the perturbation KE in a simpler framework, we consider the ssLRS model of Durran and Gingrich (2014); this is an extension of the homogeneous turbulence models developed in Lorenz (1969) and Rotunno and Snyder (2008) in which KE′ at each wavelength saturates smoothly in time instead of experiencing the abruptly truncated growth of the original Lorenz formulation. The ssLRS model is highly idealized; it neglects moist processes and relies on linearized dynamics except for the saturation criteria limiting the growth of kinetic energy perturbations. Nevertheless, some modest justification for its relevance is provided by the similarity of the ratios of variance doubling times at different resolutions given by the full convective cloud model and by the dimensional analysis of homogeneous turbulence (Table 1). In addition, the behavior of the Lorenz model is of interest in its own right because it formed the basis for the original analysis of upscale error growth.

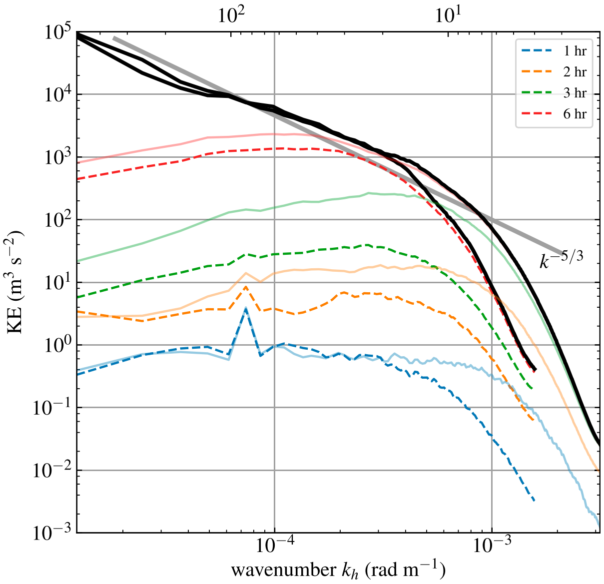

FIG. 7. Evolution of vertically averaged perturbation kinetic energy spectra $\widehat{\mathrm{KE}}'$ ($\mathrm{m^3\,s^{-2}}$) in the idealized MCS simulations using 1- (faint solid lines) and 2-km (dark dashed lines) resolutions. The thick black lines show the background $\widehat{\mathrm{KE}}$ spectrum for both the 1- and 2-km ensembles at 6 h. The solid gray line provides a background reference spectrum proportional to $k^{-5/3}$(Nastrom and Gage 1985). Initial perturbations in the moisture field are at 91 km; this wavelength is included in the 2D wavenumber bin centered at 85 km.

Consistent with observations in the mesoscales, in the ssLRS model, we impose a background KE spectrum proportional to $k^{-5/3}$, and, consistent with this choice of spectral slope, we use the surface quasigeostrophic dynamical formulation. Adjacent wavenumbers differ by a factor of $\rho = \sqrt{2}$. We retain 30 wavenumbers; the three largest correspond approximately to wavelengths of 1, 1.4, and 2 km. We run the model using 30 wavenumbers to simulate 1-km resolution and 28 wavenumbers to simulate 2-km resolution.

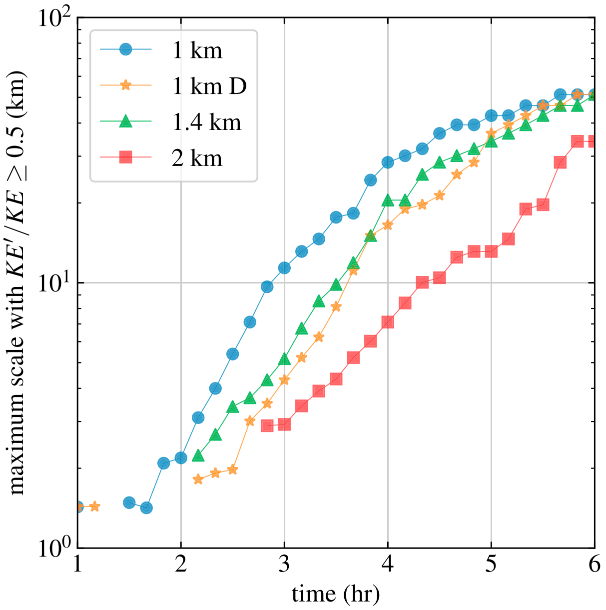

FIG. 8. Scale λ_{50} at which $\widehat{\mathrm{KE}'}/\widehat{\mathrm{KE}}$ exceeds 50% as a function of time for the 1-km (blue circles), 1-km-D (yellow stars), 1.4-km (green triangles), and 2-km (red squares) ensembles.

Figure 9a shows evolving KE$'$ spectra in the ssLRS model, comparing results at resolutions of 1- (faint solid colored lines) and 2-km (dashed colored lines) resolutions, when the initial KE$'$ is very small[6] except at wavenumber 16, which corresponds to approximately 100 km. The initial KE$'$ at wavenumber 16 has the same amplitude as the background KE at wavenumber 30. At both resolutions, the initial perturbations propagate downscale and subsequently grow upscale, with the fastest growth occurring in the shortest wavelengths, but the perturbations in the 1-km-resolution configuration grow upscale faster than those in the 2-km-resolution configuration. The smallest scale at which the KE$'$ spectra for both resolutions match also increases with time. At 1 h, the KE$'$ spectra at both resolutions are identical at all wavelengths longer than about 4 km; by 4 h, the wavelength beyond which they are identical has increased to about 20 km. At 6 h, the KE$'$ at scales of 3–4 km is saturated in the fine-resolution case, while complete saturation has not yet occurred at any wavelength in the coarse-resolution case.[7] Also of note is the decrease in KE$'$ at wavenumber 16. Negative values of KE'_{16} develop by 6 h; these nonphysical negative values arise from a flaw in Lorenz's original model that is discussed further in appendix A.

When the initial KE$'$ is only at a large scale, as in Fig. 9a, it takes some time for downscale propagation to saturate the smallest resolved scales, and saturation occurs first in the model with the finest spatial resolution. In Fig. 9b, we again compare the evolution of the KE$'$ spectra at resolutions of 1 and 2 km except that, in both cases, the initial KE$'$ is set equal to the 6-h spectral distribution of KE$'$ for the 1-km model shown in Fig. 9a.[8] KE$'$ at the smallest scales in both the 1- and 2-km models are, therefore, already saturated at $t = 0$. The subsequent evolution of the KE$'$ spectra at both resolutions is essentially identical. Taken together, the results in Figs. 9a and 9b demonstrate that using finer resolution in the ssLRS model produces more rapid KE$'$ growth though the influence of *unsaturated* perturbations in the smallest scales. Specifically, the inclusion of wavelengths smaller than any given λ_s increases the growth rate of KE$'$ at wavelengths larger than or equal to λ_s until the KE$'$ at λ_s saturates.

The resolution dependence of the spectral evolution of the unsaturated KE$'$ perturbations in Fig. 9a is similar to that shown for a dry quasigeostrophic (QG) model in Fig. 8 of Morss et al. (2009), although their perturbation amplitudes are much smaller relative to the background KE spectrum. The growth rates in Morss et al. (2009) are also much slower than those in Fig. 9a because the slope of the background KE spectrum in their model is only slightly shallower than k^{-3} and their 31-km numerical resolution is much coarser. The qualitative agreement between the ssLRS results and those obtained with the more complex dry QG model of Morss et al. (2009) encourages us to compare the ssLRS results with those from the even more complex cloud-resolving MCS simulations.

A plot of $\widehat{\mathrm{KE}'}$ spectra in the MCS simulations analogous to Fig. 9a is shown in Fig. 10, for the set of ensembles where perturbations are introduced at 4 h into the simulations, when the MCSs are well developed. The perturbation growth in the idealized MCSs ensembles parallels that of the ssLRS model in three ways. First, a rapid downscale propagation of perturbations is evident even at 1 min. Second, the growth rate of $\widehat{\mathrm{KE}'}$ at short wavelengths is more rapid in the 1-km-resolution simulations than in the 2-km simulations. Third, the smallest wavelength up to which the 1- and 2-km simulations exhibit the same values of $\widehat{\mathrm{KE}'}$ increases with time: from about 9 km at 1 min to over 20 km at 30 min and all the

---

[6] After rescaling to match the dimensional plots, the initial KE$'$ is $O(10^{-7})$ at all wavelengths.

[7] The KE$'$ growth in a 1.4-km ssLRS simulation (truncated at wavenumber 29) lies in between the coarse- and fine-resolution behaviors (not shown).

[8] To fix the negative value at wavenumber 16, discussed in appendix A, we set KE$'$ at wavenumber 16 to be the average of that at wavenumbers 15 and 17.

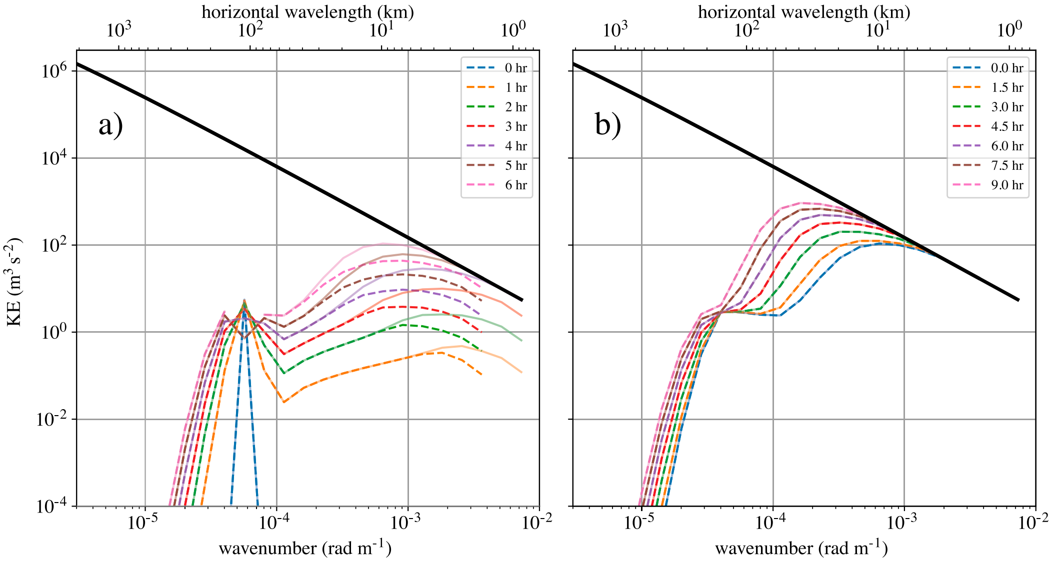

FIG. 9. Evolution of perturbation kinetic energy spectra ($m^3 s^{-2}$) generated by the ssLRS model (see text). Faint solid lines (dark dashed lines) indicate the model truncated such that 1 (2) km is the smallest resolved scale. (a) The initial KE$'$ is localized to wavenumber 16. (b) The initial KE$'$ spectrum is the 6-h spectrum at 1-km resolution from (a). The thick black line indicates the background saturation spectrum, proportional to $k^{-5/3}$.

way to the scale of the initial perturbations (91 km) at 1 h. The parallels between the perturbation KE growth in the ssLRS model and the cloud-model simulations suggest that, in both models, upscale growth from small scales that are not yet saturated produces the main difference in the $\widehat{\mathrm{KE}}'$ growth rates at different horizontal resolutions. Comparing $\widehat{\mathrm{KE}}'$ to the background $\widehat{\mathrm{KE}}$ (thick black lines) in Fig. 10 shows that the perturbation KE does not become saturated at any scale within the time period shown, suggesting that perturbations on small scales may continue to produce upscale ensemble spread in the MCS simulations longer than in the ssLRS model.

5. Conclusions

We have shown that ensemble spread grows more rapidly in simulations of idealized mesoscale convective systems as the horizontal grid spacing decreases from 2, to 1.4, and finally, to 1 km. In contrast to previous studies, in each of these cases, the numerical resolution was sufficient to reasonably represent the dynamics of deep convection. The evolution of the spread in an ensemble of 1-km-resolution simulations with increased fourth-order numerical diffusion was similar to that in the 1.4-km ensemble, demonstrating that the changes in the growth rate respond to changes in the amplitude of the shortest waves and not simply the numerical resolution per se. These results support the idea that the need for stochastic parameterization methodologies such as ECMWF-type SKEB and SCB to artificially increase ensemble dispersion (Shutts 2005; Leutbecher et al. 2017) should be reduced as the resolution of cloud-resolving ensemble prediction systems increases.

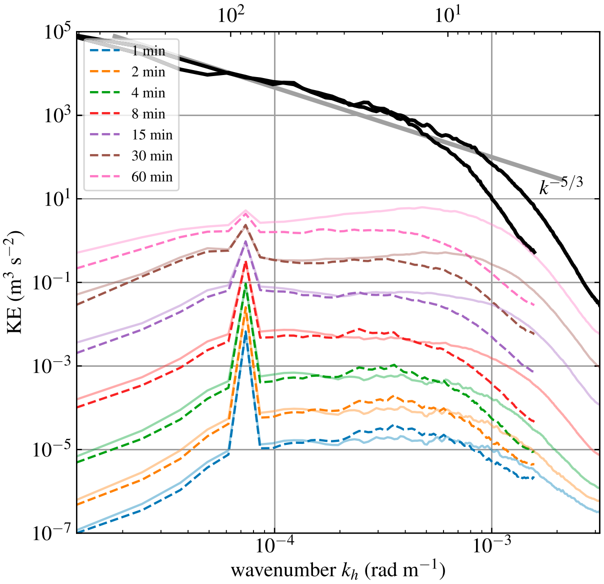

FIG. 10. Evolution of $\widehat{\mathrm{KE}}'$ ($m^3 s^{-2}$) in the idealized MCS simulations with perturbations added at 4 h into the simulations (see text). Faint solid lines (dark dashed lines) indicate the model with 1 (2)-km horizontal grid spacing. The thick black lines indicate the total KE spectrum of both the 1- and 2-km simulations averaged over 1 h (model times 4–5 h). The solid gray line indicates a background reference spectrum proportional to $k^{-5/3}$ (Nastrom and Gage 1985).

The initial perturbations were introduced at a wavelength of 91 km, rather than in the shortest scales, to ensure that they could be represented with essentially identical accuracy independent of the numerical resolution and because initial errors on such scales are a potentially important source of forecast error (Durran and Gingrich 2014). The initial perturbations spread rapidly across all scales and grew significantly on all scales. Nevertheless, over the first 3 h, the most rapid growth occurred at wavelengths smaller than roughly 30 km. The perturbation kinetic energy $\widehat{\mathrm{KE}}'$ in the smallest wavelengths grew fastest in the finest-resolution ensembles. The longest wavelength at which $\widehat{\mathrm{KE}}'$ exceeds 50% of the background KE spectrum $\widehat{\mathrm{KE}}$ was always largest in the 1-km ensemble and smallest in the 2-km ensemble. There was a systematic and statistically significant difference in the doubling time of ensemble variance across the various effective numerical resolutions. The ratios of the doubling times for pairs of ensembles of MCS simulations with numerical resolutions having ratios of 1.4:1, or 2:1, closely matched those obtained through dimensional analysis of homogeneous turbulence.

Encouraged by this similarity in the resolution dependence of the variance doubling times in our complex numerical simulations and a simple dimensional analysis of homogeneous turbulence models, we examined KE′ growth as a function of numerical resolution in the ssLRS model (Lorenz 1969; Rotunno and Snyder 2008; Durran and Gingrich 2014). The ssLRS model responded to an initial large-scale perturbation with scale-dependent error growth grossly similar to that in our MCS simulations. In particular, the perturbations in the ssLRS model spread rapidly downscale from an initial 100-km wavelength and subsequently grew back upscale, with more rapid growth in the calculations corresponding to the higher-numerical-resolution ensemble.[9] Our results are also similar to those obtained by Morss et al. (2009) using a dry quasigeostrophic model at multiple horizontal resolutions, whose underlying dynamics are much closer to those in the ssLRS model than are the dynamics governing our cloud-resolving model for deep convection. Despite their varying dynamical complexity, all three systems show more rapid KE′ growth at finer resolution.

Let us now return to the question posed in the introduction about the influence of numerical resolution on upscale perturbation growth when the initial perturbation KE′ follows the dashed orange curve in Fig. 1. As demonstrated in Fig. 9b, there will be no difference in the rate of ensemble spread between the fine- and coarse-resolution cases because the initial KE′ is saturated throughout all the smallest scales, including both the 1- or 2-km cutoff wavelengths. Nevertheless, many recent studies have found that the KE′ spectrum in actual ensemble forecasts grows primarily up-amplitude rather than as an upscale cascade like that in Fig. 1 (Mapes et al. 2008; Durran and Gingrich 2014; Durran and Weyn 2016). In such cases, the small-scale KE′ saturates rather slowly, and the situation shown in Fig. 1 does not apply; instead, one would expect more opportunity for unsaturated small-scale KE′ to influence larger scales and therefore more rapid ensemble spread in higher-resolution simulations. This up-amplitude growth appears to slow the saturation of KE′ at the smallest scales in the our ensemble simulations of MCS, thereby leading to our basic result that the ensemble spread grows more rapidly at higher resolution.

TABLE 2. Evolution of perturbation KE at wavenumber 16 (KE'_{16}), where the initial error was introduced, in the ssLRS model shown in Fig. 9a.

Time (h)	KE'_{16} ($\mathrm{m^3\,s^{-2}}$)
0	5.597
1	5.332
2	4.574
3	3.438
4	2.090
5	0.725
6	−0.459

Acknowledgments. This research is funded by Grants N000141410287 and N000141712660 from the Office of Naval Research (ONR). J. A. Weyn was partly supported by the Department of Defense (DoD) through the National Defense Science and Engineering Graduate (NDSEG) Fellowship Program. The simulations were conducted on Gordon, a supercomputer at the Navy DoD Supercomputing Resource Center (DSRC). The authors gratefully acknowledge the comments of Chris Snyder and two anonymous reviewers, which have greatly improved this manuscript.

APPENDIX A

A Flaw in the Lorenz Model

The experiment in Fig. 9a reveals a flaw in the Lorenz model. The perturbation kinetic energy at wavenumber bin 16 (KE'_{16}), where the initial error was isolated, decreases over time, especially at 4 h and beyond, becoming negative at 6 h (the value at this time is not plotted on the logarithmic axis). Values for KE'_{16} are listed for hours 1–6 in Table 2, which were obtained by integrating the ssLRS system using MATLAB's

---

[9] These simulations also revealed a flaw in the original Lorenz model that is discussed in appendix A.

ode45 routine with an absolute error tolerance equal to 10^{-6} times the background saturation KE spectrum. Negative values of KE'_k (which is proportional to the sum of the magnitude squared of the Fourier transform of the horizontal perturbation velocity components at wavenumber k) are not correct and must arise from inaccuracies in some combination of the closure approximations used in Lorenz's model and the numerical calculations of the coefficient values for that model.

The evolution of KE′ in the Lorenz system is governed by the system of second-order differential equations:

$$\frac{d^2 Z_k}{dt^2} = \sum_{l=1}^{n} C_{k,l} Z_l, \tag{A1}$$

where the Z_k (the error) is the ensemble-average KE′ about the ensemble mean integrated with respect to the logarithm of the wavenumber over the kth wavenumber bin, $\mathbf{C}$ is a constant matrix governing scale interactions, and n is the number of wavenumber bins in the model (Lorenz 1969; Rotunno and Snyder 2008). The values of $\mathbf{C}$ are negative along the diagonal, indicating that, for a positive error at wavenumber bin k, the tendency of the rate of error growth is negative. In the absence of sufficiently large errors at adjacent wavenumbers, this produces an initial decrease in Z_k. When $C_{k,k}$ is sufficiently negative, initial errors concentrated at a single wavenumber k will temporarily generate negative values of Z_k. Once Z_k becomes negative, the sign of the second derivative reverses in (A1), and the sign of Z_k eventually reverses back to positive, avoiding the problem at later times when the errors are more widespread in spectral space.

As evident in Lorenz (1969) and in Tables 1–4 of Rotunno and Snyder (2008), the entries on the main diagonal of the $\mathbf{C}$ matrix are negative for all combinations of $k^{-5/3}$ and k^{-3} background KE spectra and for either barotropic vorticity or surface quasigeostrophic dynamics.[A1] In contrast to the total KE, KE′ is not conserved, and it does not spread to adjacent wavenumbers by simple advection and diffusion. One might wonder if the diagonal entries in $\mathbf{C}$ should be nonnegative, which would be a sufficient, but not a necessary, condition to ensure KE′ remained positive definite in every wavenumber bin at all stages of the integration.

At least for single wavenumbers, as opposed to averages over bins, one can rigorously show that the ensemble average kinetic energy $\overline{e_{\mathbf{K}} e_{-\mathbf{K}}}$ of an error present *only* at one isolated 2D wavenumber $\mathbf{K}$ should remain unchanged using expressions from earlier steps in Lorenz's derivation. If error is present only at a single wavenumber, (19) of Lorenz (1969) reduces to

$$\frac{d^2(\overline{e_{\mathbf{K}} e_{-\mathbf{K}}})}{dt^2} = 4\widetilde{S_0 S_0} A^2_{\mathbf{K},\mathbf{K}} \overline{e_{\mathbf{K}} e_{-\mathbf{K}}},$$

but by Lorenz's (13), $A_{\mathbf{K},\mathbf{K}}$ is zero, so there should be no change in $\overline{e_{\mathbf{K}} e_{-\mathbf{K}}}$. To interpret this result, note that except for an ad hoc treatment of nonlinear saturation, the Lorenz model is linear, and it estimates the influence of triad interactions that produce forcing at wavenumber $\mathbf{K}$ via interactions with perturbations at wavenumber $\mathbf{L}$ and mean-state fluctuations at wavenumber $\mathbf{M} = \mathbf{K} - \mathbf{L}$. When $\mathbf{K} = \mathbf{L}$, the mean-state wavenumber involved in the interaction is $\mathbf{M} = 0$. Since the wavenumber-0 background flow vanishes in the isotropic system assumed by Lorenz, interactions with it cannot change the error amplitude.

While the single-wavenumber analysis suggests that $C_{k,k}$ should be zero, this result does not directly apply to Lorenz's equation set, which is averaged over wavenumber bins, because (A1) is obtained by assuming the background and error energies vary smoothly with the magnitude of the wavenumber and that $Z(\mathbf{K})$ can be treated as a constant when averaging Lorenz's (27) over each wavenumber bin. Evidence that $C_{k,k}$ can be negative is provided by Leung (2017, their Fig. 3.2), who conducted simulations of ensemble error growth in homogeneous, isotropic turbulence with a surface quasigeostrophic spectral model, bin averaged the results, and found that the error can decrease in individual bins as part of a short-term initial adjustment. If, in our experiments with the ssLRS model, we empirically modify only $C_{16,16}$ to be less negative, we find that multiplication by a factor less than or equal to 0.763 is sufficient to ensure that the initial adjustment never drives Z_{16} negative. Similar empirical tests at other wavenumbers suggest that reducing the magnitude of all the diagonal elements to about 0.74 of their original value would be enough to avoid the development of negative Z_k when the initial KE′ is concentrated entirely in one arbitrary wavenumber bin. Of course these empirical experiments only establish that it is not necessary for $C_{k,k}$ to be nonnegative to avoid initial short-term negative values for some initial distributions of Z_k. Further research to definitively establish the correct values for $C_{k,k}$ would be welcome.

APPENDIX B

Comparison of 2.8-km-Resolution MCS Simulations to the Rest

An ensemble of simulations of MCSs with horizontal grid spacing of 2.8 km was also constructed; the results

---

[A1] A few positive entries appear in these tables where Lorenz assumed the background KE started dropping toward zero at planetary-scale wavelengths.

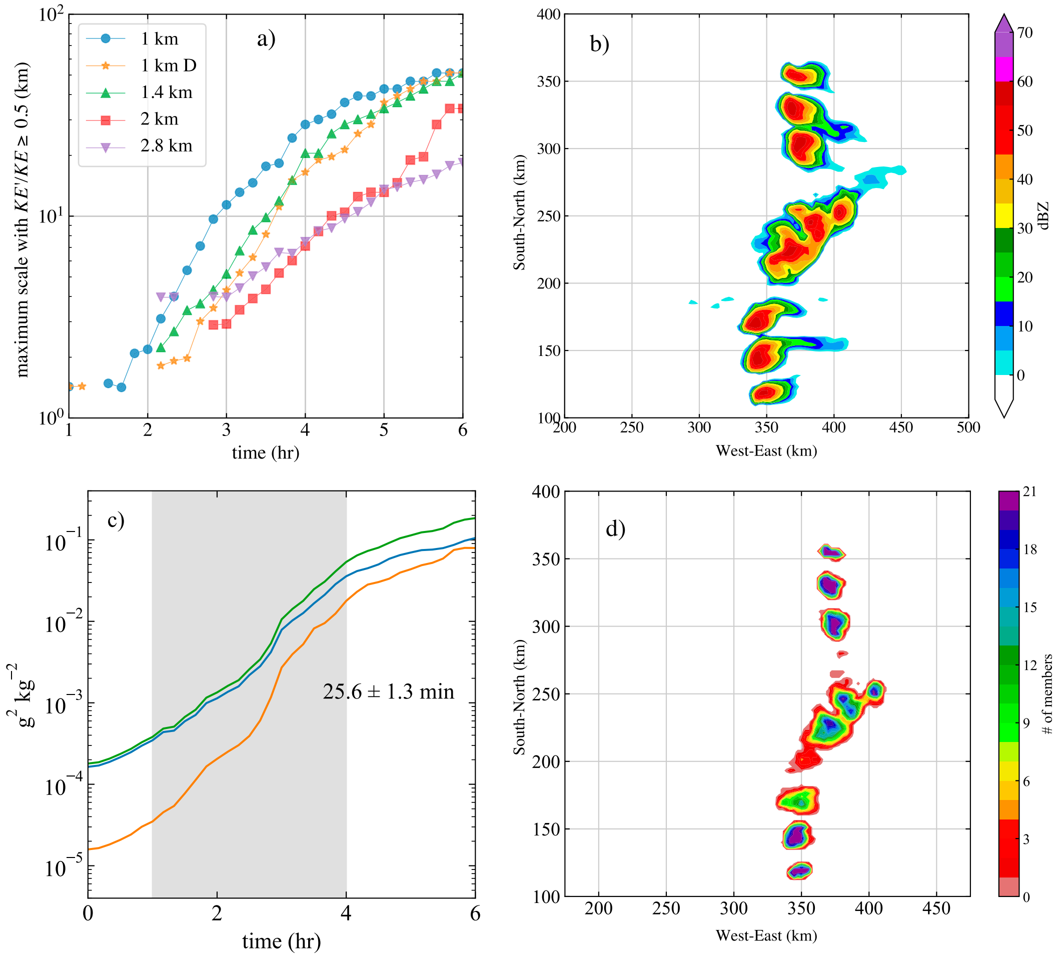

FIG. B1. Additional results for the ensemble with 2.8-km resolution. (a) As in Fig. 8, but including results from the 2.8-km simulations. (b) As in Fig. 2, but for model-simulated composite reflectivity at 5 h. (c) As in Fig. 5, but for domain-averaged Var(q_v) (blue), Bias^2(q_v) (orange), and MSD(q_v) (green). (d) As in Fig. 3, but for number of ensemble members with synthetic reflectivity at or above 45 dBZ.

from this ensemble are shown in Fig. B1. The ensemble agreement at $t = 5$ h into the simulations for this ensemble (Fig. B1d) is qualitatively similar to that of the 2-km ensemble (Fig. 3f) except for one prominent cell that only has 16-member agreement at best. In contrast to the dependence on grid spacing in the finer-resolution cases, the variance growth rates relative to those in the 2-km ensemble did not significantly slow down. As shown in Fig. B1c, the variance doubling time at 2.8-km grid spacing was 25.6 ± 1.8 min, or nearly identical to that of the 2-km ensemble, and well within the error bounds. The modest change in the 2.8-km case is further illustrated by the evolution of λ_{50} with time shown in Fig. B1a, which is identical to Fig. 8 except that the 2.8-km ensemble has been added. At early times, λ_{50} is longer in the 2.8-km ensemble than in the 2-km ensemble, although by hour 6, it has become substantially shorter.

We hypothesize that the 2.8-km grid is coarse enough to change the scaling of the perturbation growth rates by modifying the structure and growth of the convective elements. (One would certainly expect a major change in the fidelity of convective simulations, and therefore perturbation growth rates, at very coarse resolutions like 10 km.) Some brief quantitative support for this hypothesis is provided by the absolute maximum in both time and space of the updraft velocity in the control members of each ensemble. The maximum updraft velocity gradually decreases from 41.8 to 34.3 m s^{-1} as the resolution is coarsened from 1 to 2 km, but the maximum updraft velocity of the 2.8-km control simulation is only 24.4 m s^{-1}, a steep decline. The simulation with 2.8-km resolution is substantially reducing the updraft velocities and therefore not realistically representing the strong convection.

REFERENCES

Buizza, R., M. Miller, and T. N. Palmer, 1999: Stochastic representation of model uncertainties in the ECMWF ensemble prediction system. *Quart. J. Roy. Meteor. Soc.*, **125**, 2887–2908, https://doi.org/10.1002/qj.49712556006.

——, P. L. Houtekamer, G. Pellerin, Z. Toth, Y. Zhu, and M. Wei, 2005: A comparison of the ECMWF, MSC, and NCEP global ensemble prediction systems. *Mon. Wea. Rev.*, **133**, 1076–1097, https://doi.org/10.1175/MWR2905.1.

Clark, A. J., W. A. Gallus, M. Xue, and F. Kong, 2009: A comparison of precipitation forecast skill between small convection-allowing and large convection-parameterizing ensembles. *Wea. Forecasting*, **24**, 1121–1140, https://doi.org/10.1175/2009WAF2222222.1.

——, ——, ——, and ——, 2010: Growth of spread in convection-allowing and convection-parameterizing ensembles. *Wea. Forecasting*, **25**, 594–612, https://doi.org/10.1175/2009WAF2222318.1.

Durran, D. R., and M. Gingrich, 2014: Atmospheric predictability: Why butterflies are not of practical importance. *J. Atmos. Sci.*, **71**, 2476–2488, https://doi.org/10.1175/JAS-D-14-0007.1.

——, and J. A. Weyn, 2016: Thunderstorms do not get butterflies. *Bull. Amer. Meteor. Soc.*, **97**, 237–243, https://doi.org/10.1175/BAMS-D-15-00070.1.

——, ——, and M. Q. Menchaca, 2017: Practical considerations for computing dimensional spectra from gridded data. *Mon. Wea. Rev.*, **145**, 3901–3910, https://doi.org/10.1175/MWR-D-17-0056.1.

Hohenegger, C., and C. Schär, 2007: Atmospheric predictability at synoptic versus cloud-resolving scales. *Bull. Amer. Meteor. Soc.*, **88**, 1783–1793, https://doi.org/10.1175/BAMS-88-11-1783.

Leung, T. Y., 2017: Role of initial and model errors in uncertainty of weather forecasts. M.S. thesis, Dept. of Mathematics of Planet Earth Centre for Doctoral Training, Imperial College London and University of Reading, 46 pp.

Leutbecher, M., and Coauthors, 2017: Stochastic representations of model uncertainties at ECMWF: State of the art and future vision. *Quart. J. Roy. Meteor. Soc.*, **143**, 2315–2339, https://doi.org/10.1002/qj.3094.

Lilly, D. K., 1972: Numerical simulation studies of two-dimensional turbulence: II. Stability and predictability studies. *Geophys. Fluid Dyn.*, **4**, 1–28, https://doi.org/10.1080/03091927208236087.

Lorenz, E. N., 1969: The predictability of a flow which possesses many scales of motion. *Tellus*, **21**, 289–307, https://doi.org/10.3402/tellusa.v21i3.10086.

Mapes, B., S. Tulich, T. Nasuno, and M. Satoh, 2008: Predictability aspects of global aqua-planet simulations with explicit convection. *J. Meteor. Soc. Japan*, **86A**, 175–185, https://doi.org/10.2151/jmsj.86A.175.

Morss, R. E., C. Snyder, and R. Rotunno, 2009: Spectra, spatial scales, and predictability in a quasigeostrophic model. *J. Atmos. Sci.*, **66**, 3115–3130, https://doi.org/10.1175/2009JAS3057.1.

Nastrom, G. D., and K. S. Gage, 1985: A climatology of atmospheric wavenumber spectra of wind and temperature observed by commercial aircraft. *J. Atmos. Sci.*, **42**, 950–960, https://doi.org/10.1175/1520-0469(1985)042<0950:ACOAWS>2.0.CO;2.

Palmer, T. N., A. Döring, and G. Seregin, 2014: The real butterfly effect. *Nonlinearity*, **27**, R123–R141, https://doi.org/10.1088/0951-7715/27/9/R123.

Raftery, A. E., T. Gneiting, F. Balabdaoui, and M. Polakowski, 2005: Using Bayesian model averaging to calibrate forecast ensembles. *Mon. Wea. Rev.*, **133**, 1155–1174, https://doi.org/10.1175/MWR2906.1.

Rotunno, R., and C. Snyder, 2008: A generalization of Lorenz's model for the predictability of flows with many scales of motion. *J. Atmos. Sci.*, **65**, 1063–1076, https://doi.org/10.1175/2007JAS2449.1.

Schwartz, C. S., G. S. Romine, K. R. Smith, and M. L. Weisman, 2014: Characterizing and optimizing precipitation forecasts from a convection-permitting ensemble initialized by a mesoscale ensemble Kalman filter. *Wea. Forecasting*, **29**, 1295–1318, https://doi.org/10.1175/WAF-D-13-00145.1.

Shutts, G., 2005: A kinetic energy backscatter algorithm for use in ensemble prediction systems. *Quart. J. Roy. Meteor. Soc.*, **131**, 3079–3102, https://doi.org/10.1256/qj.04.106.

——, 2015: A stochastic convective backscatter scheme for use in ensemble prediction systems. *Quart. J. Roy. Meteor. Soc.*, **141**, 2602–2616, https://doi.org/10.1002/qj.2547.

Weyn, J. A., and D. R. Durran, 2017: The dependence of the predictability of mesoscale convective systems on the horizontal scale and amplitude of initial errors in idealized simulations. *J. Atmos. Sci.*, **74**, 2191–2210, https://doi.org/10.1175/JAS-D-17-0006.1.

Zhang, F., C. Snyder, and R. Rotunno, 2003: Effects of moist convection on mesoscale predictability. *J. Atmos. Sci.*, **60**, 1173–1185, https://doi.org/10.1175/1520-0469(2003)060<1173:EOMCOM>2.0.CO;2.

——, N. Bei, R. Rotunno, C. Snyder, and C. C. Epifanio, 2007: Mesoscale predictability of moist baroclinic waves: Convection-permitting experiments and multistage error growth dynamics. *J. Atmos. Sci.*, **64**, 3579–3594, https://doi.org/10.1175/JAS4028.1.